Rare Metal Materials and Engineering
Volume 54, Issue 5, May 2025
Available online at www.rmme.ac.cn

Science Press

Cite this article as: Zhang Lei, Huang Bensheng, Xie Chuandi, et al. Preparation and High-Temperature Oxidation Performance of TiC-NiCr Cermet[J]. Rare Metal Materials and Engineering, 2025, 54(05): 1194-1206. DOI: https://doi.org/10.12442/j.issn.1002-185X.20240198.

ARTICLE

Preparation and High-Temperature Oxidation Performance of TiC-NiCr Cermet

Zhang Lei[1,2,4], **Huang Bensheng**[1], **Xie Chuandi**[2,4], **Chen Gen**[5], **Du Jiao**[2,4], **Sun Haishen**[2,3,4], **Zuo Hanyang**[6]

[1] School of New Energy and Materials, Southwest Petroleum University, Chengdu 610500, China; [2] Shandong Province Key Laboratory of Powder Metallurgy and Advanced Manufacture, Jinan 271100, China; [3] University of Science & Technology Beijing, Beijing 100083, China; [4] Department of Intelligent Manufacturing, Laiwu Vocational and Technical College, Jinan 271100, China; [5] Kunshan EMI Pipeline Tech. Co., Ltd, Kunshan 215300, China; [6] Material Corrosion and Protection Key Laboratory of Sichuan Province, Zigong 643002, China

Abstract: Powder metallurgy was used to fabricate TiC-NiCr cermets and the oxidation behavior at 900 °C was investigated. Results reveal that TiC-NiCr cermets have uniform structures with excellent mechanical properties, whose hardness is 65 HRC and flexural strength is 1450 MPa. The high-temperature oxidation mechanism of TiC-based cermets was investigated through an X-ray diffractometer and scanning electron microscope. The added elements Ni and Cr along with their solid solutions not only bond with the hard phase TiC to ensure the physical performance of the cermet, but also impede the internal diffusion during oxidation by forming a dense composite oxide layer, thereby enhancing the oxidation resistance. The TiC-NiCr cermet exhibits a dense protective oxide layer at 900 °C and can endure continuous oxidation for approximately 1000 h. A methodology for fabricating TiC-NiCr metal matrix composites is proposed, and their oxidation resistance is evaluated, providing a theoretical and practical basis for simultaneously enhancing the mechanical properties and oxidation resistance and reducing production costs.

Key words: TiC-NiCr; microstructure; high-temperature oxidation; thermodynamics and kinetics

1 Introduction

Cermets are heterogeneous composite materials composed of a mixture of one or more ceramic phases with metal, where the proportion of the ceramic phase is typically 10vol%–90vol% of the material volume. These composites exhibit a unique combination of metallic properties, including good toughness, electrical conductivity, and thermal conductivity, and ceramic characteristics, such as high strength, hardness, wear resistance, high-temperature stability, and excellent chemical stability. Consequently, they have emerged as crucial structural materials with diverse and extensive applications. Cermets are classified into various types based on their ceramic phases: carbide, oxide, carbonitride, boride-based material, and graphite or diamond-like carbon[1–5]. Oxide-based metal ceramics, composed of oxides (alumina, zirconia, or their composites) as the hard phase and metals or alloys as the bonding phases, represent heterogeneous composite materials. The materials in this category typically exhibit high hardness and good thermal stability, showing significant application potential in aerospace, automotive manufacturing, medical devices, electronic components, and other fields[6]. Carbonitride-based cermets, which are developed based on the foundation of carbide-based cermets, have emerged as a new class of cermet, exhibiting high hardness, high strength, excellent high-temperature resistance, fine wear resistance, good toughness, low density, and high thermal conductivity. Currently, these materials have been used in widespread applications, such as machining, high-temperature components in engines, and sealing elements in the petroleum industry[7–11]. It has been reported that the metal borides possess high thermal conductivity and temperature stability,

---

Received date: April 03, 2024
Foundation item: National Natural Science Foundation of China (52376076); Open Fund of Material Corrosion and Protection Key Laboratory of Sichuan Province (2023CL13); Laiwu Vocational and Technical College Teacher's Research Fund (2023jsky05)
Corresponding author: Huang Bensheng, Ph. D., Professor, School of New Energy and Materials, Southwest Petroleum University, Chengdu 610500, P. R. China, E-mail: hbslxp@163.com

making them suitable for applications requiring excellent wear resistance, such as cutting tools, rock drilling tools, and wear-resistant components. However, owing to their low strength and high brittleness, these materials are unsuitable for use under impact loads[12–14]. Graphite-metal composite materials are employed in various electrical contacts and are extensively used for manufacturing brake linings and clutch facings. Additionally, the diamond-like carbon of coarse fragments or fine powders within a metal matrix is usually used for the production of cermets in the application of grinding, polishing, sawing, cutting, dressing, and shaping tools[15–17]. Carbide-based cermets primarily consist of metals and carbides. These materials typically exhibit outstanding thermal, mechanical, and chemical stabilities, making them widely applicable in high-temperature, high-pressure, and corrosive environments. Among these materials, tungsten carbide-based and titanium carbide-based cermets have a long development history and a broad range of applications[18].

WC-Co cermet possesses the most favorable composition and optimal atomic interactions, considering the mechanical performance. The crystal structure of WC is cubic with carbon atoms forming covalent bonds with tungsten atoms, providing high hardness and excellent wear resistance. The role of Co is to consolidate and bond tungsten carbide particles, contributing to high toughness and ductility. The crystal structure of Co is a close-packed hexagonal structure and it remains stable at room temperature. The bonding between Co and WC is facilitated by the plastic deformation ability of Co, which promotes the gap filling between WC particles and forms strong connections. Metal-metal and metal-nonmetal bonds simultaneously exist between Co and WC. Owing to the combination of covalent bonding in WC and metallic and nonmetallic bonding in Co, WC-Co alloys exhibit excellent mechanical properties, such as high hardness, toughness, and wear resistance. These intricate atomic interactions impart unique properties to WC-Co alloys, making them crucial materials for numerous industrial applications[19–24]. However, such alloys are rare due to the excessive exploitation of resources. Additionally, the critical element Co primarily coexists with minerals, such as nickel, copper, manganese, and iron. Insufficient geological reserves, low-grade deposits, and production difficulties in Co resources in China have also highlighted a need to develop cost-effective cermets without tungsten and Co, which have significant economic and strategic importance[25–27]. In addition, WC can undergo oxidation at high temperatures, which may affect its performance. Preventative measures, such as special protective coatings or alloying, are required when WC is used in oxidizing environments. Yan et al[28] found that adding WB to WC-Co can lead to the in-situ formation of WCoB. Thermal analysis demonstrated that the high-temperature oxidation resistance of WCoB surpassed that of WC and Co, suggesting that adding WB can significantly enhance the high-temperature oxidation resistance of WC-Co.

TiC has a high melting point (3250 °C), compared with WC (2870 °C), exhibiting excellent wear resistance. Its density is 4.93 g/cm^3, which is only approximately one-third of that of WC (15.63 g/cm^3) [29]. Compared with tungsten resources, titanium resources are more abundant on the earth, and their production costs are relatively low[30–32]. At elevated temperatures, TiC forms a stable titanium oxide layer in the oxidizing atmosphere, providing a certain level of protection and slowing down further oxidation of the material. Consequently, TiC often exhibits superior oxidation resistance in high-temperature applications[33]. TiC typically demonstrates better oxidation resistance at high temperatures than WC.

TiC-NiCr cermets represent a novel class of materials characterized by high-temperature resistance, wear resistance, corrosion resistance, and a balanced combination of toughness, strength, and thermal conductivity. Studies have demonstrated that incorporating other metals into the Ni-bonding-phase metal can enhance the high-temperature strength. NiCr, which serves as the bonding phase against the hard phase, not only exhibits good wettability but also considerably improves toughness, high-temperature strength, oxidation resistance, and corrosion resistance[34–36].

Currently, the preparation and high-temperature performance of TiC-based metal ceramics using NiCr as the sole bonding phase are rarely reported. In this research, the powder metallurgy process used to manufacture metal ceramics was optimized. TiC-NiCr metal ceramics with uniform structures and excellent properties were prepared. In addition, this research focused on the high-temperature oxidation of TiC-based metal ceramics. The experiment conditions of previous studies are usually temperatures below 800 °C and durations under 100 h[37–39]. Therefore, this investigation prolongs the duration to 1000 h and increases the temperature to 900 °C. The long-term oxidation resistance of TiC-NiCr metal ceramics at elevated temperatures provides valuable insights for material performance assessment, enhancement of oxidation resistance, industrial manufacturing, energy conservation, environmental protection, material selection and design, and research on protective materials.

2 Experiment

2.1 Raw materials and specimen preparation

In this study, experiments were conducted using TiC, Ni, and Cr powders as the raw materials. The average particle size of the raw materials is below 50 μm with the oxygen content below 0.5wt%. The composition is listed in Table 1.

The powder was uniformly mixed using a combination of dry mixing and wet grinding methods, as shown in Fig.1. For the dry mixing process, the pre-prepared powders, as specified in the composition table, were introduced into an automatic mixer and mixed for 2 h. The wet grinding process involved the use of an XGP36X planetary ball mill, with the addition of high-speed steel balls and anhydrous ethanol during the wet grinding process, at a ball-to-material ratio of 3:1 and a liquid-to-solid ratio of 2:5.

After wet grinding for 24 h, the slurry was discharged and sieved through a sieve of 380 μm. Subsequently, the material

Table 1 Chemical composition and particle size D_{50} of raw materials

Raw material	TiC	Cr	Ni
Content/wt%	60	10	30
D_{50}/μm	11.81	38.59	11.58

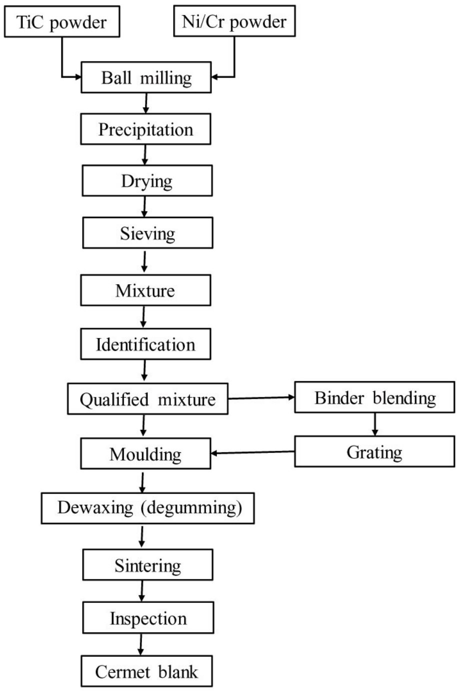

Fig.1 Process flow diagram

was dried in a vacuum oven at 65 °C for 8 h, followed by sieving through a sieve of 250 μm. To facilitate subsequent compaction and molding, a certain proportion of polymer binder was added, mixed thoroughly, and dried again. The resulting material was sieved through a sieve of 380 μm and kept for further use. Compaction and molding were performed using a Y41-63 type 60 t single-column hydraulic press, and the specimens were then subjected to vacuum sintering in a ZTS-40/40/80 integrated vacuum sintering and debonding furnace. The maximum sintering temperature was 1420 °C and the insulation period was 40 min. A TiC-NiCr cermet composite was obtained after testing. After sintering, the dimensions of the specimens were Φ20 mm×40 mm. Fig. 1 shows the process flow chart.

The sintering process of TiC-NiCr cermet is a thermal processing technique involving a series of physical and chemical transformations, transforming agglomerates of powder into aggregates of grains and ultimately yielding a product with the desired physicochemical properties. Consequently, the sintering process plays a crucial role in determining the performance of the final product. The sintering temperature profile of TiC-NiCr cermet in this experiment is shown in Fig.2.

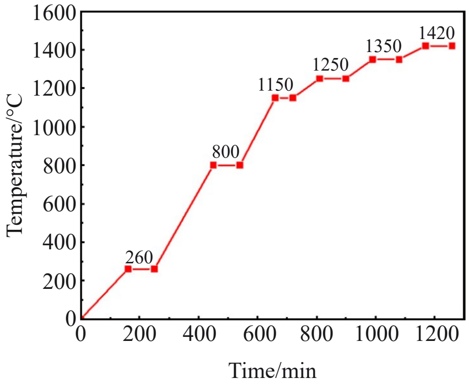

Fig.2 Temperature of sintering process

2.2 Performance testing and microstructure analysis

2.2.1 Mechanical property

After mechanical polishing of the specimens, the density was measured using an ES-J200D density balance. The hardness was determined using an HR-150A Rockwell hardness tester, and the flexural strength was assessed using a three-point bending test on a HAW-1000D universal testing machine. Typically, the processed specimens with dimensions of 30 mm×5 mm×5 mm were positioned on a universal testing machine for three-point bending strength testing, and the test parameters were set as the span of 20 mm and the loading rate of 0.05 mm/min. The principles of the three-point bending strength experiment are shown in Fig.3.

Three-point bending strength calculation formula is as follows:

$$\sigma = \frac{3PL}{2bh^2} \tag{1}$$

where σ represents the flexural strength (MPa), P is the maximum load (N), L is the span (mm), b is the specimen width (mm), and h is the specimen thickness (mm). The flexural strengths of the cermet specimens were determined using the three-point bending method.

2.2.2 Oxidation mechanism experiment

The purpose of oxidation experiments was to investigate the oxidation mechanisms and reaction kinetics of materials under various conditions, such as temperature, pressure, and gas composition. Place a specimen of known mass and surface area in an air atmosphere, and heat it for a specific duration. Then, remove the specimen for cooling, and weight the specimen to determine the extent of oxidation. The

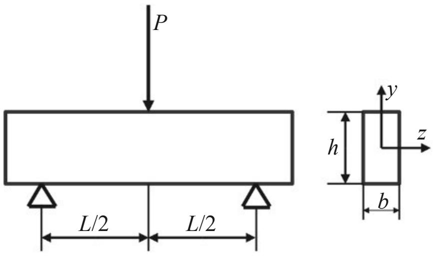

Fig.3 Schematic diagram of flexural strength experiment

morphologies of the oxidized specimens were observed and characterized using X-ray diffraction (XRD) and scanning electron microscopy (SEM).

The oxidation reaction of metals is typically initiated by the formation of an oxide layer on the metal surface. Therefore, the process of metal oxidation generally encompasses two stages: the formation stage and the growth stage of oxide layer. The formation stage of the oxide layer primarily includes oxygen adsorption on the metal surface, nucleation of oxide species, lateral growth of oxide nuclei, and the development of a tightly adherent oxide layer. After the formation of an exceedingly thin oxide layer on the surface, as oxidation proceeded, the oxide layer entered the growth stage. Based on the aforementioned mechanism, the specimens were polished with 2000# sandpaper after cutting, followed by ultrasonic cleaning in anhydrous ethanol and subsequent drying. The specimens were then placed in pre-weighed Al_2O_3 crucibles and subjected to cyclic oxidation experiments in an OTF-1200X tubular resistance furnace. The temperature was set at 900 °C, and the duration was 1000 h. The specimens were removed from the furnace every 100 h and cooled to room temperature in ambient air. Their masses were measured using an electronic balance with an accuracy of 0.01 mg. The increase in the oxidation mass per unit area was calculated, and three specimens were tested for each alloy composition to obtain the average value for analysis.

Surface phase analysis of the oxidized specimens was performed using a D8 ADVANCE XRD (Bruker). The surface and cross-section morphologies of the oxide layers were observed using an EVO10 field-emission SEM. The micro-area composition analysis was conducted using an energy-dispersive spectrometer (EDS).

3 Results

3.1 TiC-NiCr microstructure

3.1.1 Microstructure

A typical structure of the TiC-NiCr cermet after vacuum sintering is shown in Fig.4. The TiC ceramic phase exhibits an irregularly shaped, nearly spherical or square morphology. In contrast, the NiCr metal phase is uniformly distributed. The microstructure of the TiC-NiCr cermet reveals that small ceramic-phase particles are evenly dispersed within the continuous NiCr metal phase. The metal phase forms a continuous matrix that encapsulates the uniformly distributed ceramic particles. The particle size of the TiC ceramic phase is approximately 5–10 μm. Fig.5 shows SEM image and corresponding EDS elemental surface distribution maps, which clearly illustrate the distribution of TiC particles within the metal bonding phase. The TiC particles are distinctly surrounded by Ni and Cr. Particularly, Ni exhibits enrichment in a circular pattern around the TiC particles. The distribution of Cr is relatively scattered, and it is reported that a portion of Cr forms a face-centered cubic Ni(Cr) solid solution, whereas other Cr exists in elemental form.

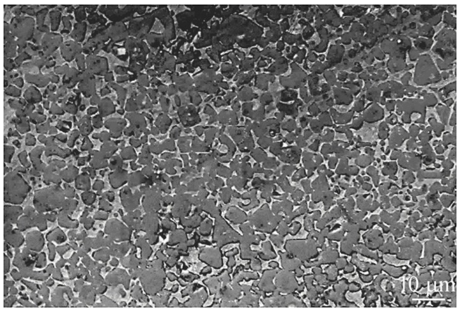

Fig.4 Microstructure of TiC-NiCr cermet

3.1.2 Formation mechanism of microstructure

Sintering of metal ceramics falls under the category of liquid phase sintering. Liquid phase sintering can be divided into three stages with indistinct boundaries: (1) the generation of the liquid phase and particle rearrangement; (2) the dissolution/precipitation of the solid phase (solid-phase diffusion, grain growth, and shape adjustment); (3) the formation of a solid-phase framework (elimination of pores, grain growth, and contact enlargement). The evolution of microstructural changes and densification behavior varies across these stages, as shown in Fig.6[40], and the proportions

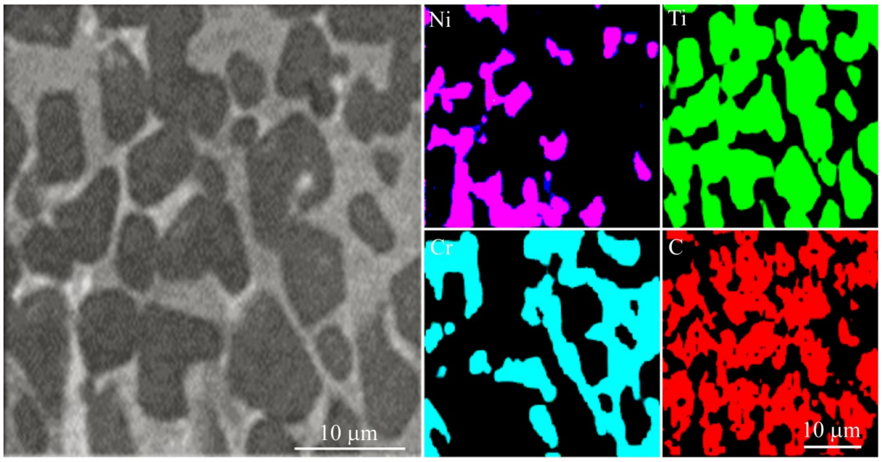

Fig.5 SEM image and EDS element mapping of TiC-NiCr cermet

of each stage are influenced by various factors, such as particle size, particle shape, heating rate, density, and particle composition. In TiC-NiCr cermet, the overall sintering process can be devided into the following four stages. The first stage occurs below 800 °C, and it can be further subdivided into the pre-sintering stage (0 – 260 °C) and the degreasing sintering stage (260 – 800 °C), which involves the removal of the easily sintered volatile binder from the green compact, as shown in Fig. 6. In this stage, the primary chemical transformations involve the gradual decomposition and carbonization of the polymer binder within the compact under heating with a slow expulsion through the interparticle pores. During this stage, the state of the powder particles changes, initiating the surface diffusion and enhancing the compaction strength. This stage has a relatively slow heating rate primarily to prevent rapid carbonization reactions and volatilization of the binder, which can lead to the formation of internal voids and defects, thereby affecting the final density of the sintered product.

The second stage occurs between 800 and 1280 °C (eutectic temperature), which shows the liquid formation and particle rearrangement in the cermet powder, as depicted in Fig. 6. Within this temperature range, Ni liquid phase gradually forms as the temperature increases, facilitating the surface diffusion and volume diffusion between the TiC particles. The solid-phase particles of TiC and Cr exist at suspended state within the Ni liquid phase, which is driven by the surface tension of the liquid phase, leading to a gradual reduction in the distance between the TiC particles and rapid densification. With the increase in temperature, the diffusion of Ni intensifies, bringing the TiC particles closer together and resulting in substantial volume shrinkage of the sintered specimen. Meanwhile, the solubility of Cr in Ni gradually increases, leading to the formation of more Ni-Cr solid solution.

The third stage occurs between 1280 (eutectic temperature) and 1380 °C (sintering temperature), which shows the solid-phase dissolution-precipitation stage, as shown in Fig. 6. Within this sintering temperature range, a significant amount of the liquid phase appears. Simultaneously, the TiC grains form a skeletal structure in the liquid phase of the Ni-Cr solid solution, initiating the contraction of the blank and forming the primary organizational framework. During this process, a thin layer of liquid phase is formed on the surface of Ni-Cr, providing lubrication between the TiC particles and reducing the friction between them. Under the influence of liquid phase surface tension, TiC particles are prone to rearrangement, further enhancing densification. During this sintering process, dissolution-precipitation phenomena also occur because of the high surface energy of the local TiC particles. Under these sintering temperature conditions, the TiC particles easily dissolve in the liquid phase and are precipitated in other regions. Consequently, this result leads to the preferential growth of TiC grains along a specific direction. This growth pattern promotes bonding or aggregation among adjacent TiC grains, causing a gradual transformation of the grain morphology into a spherical shape. Simultaneously, smaller grains diminish or disappear, whereas larger grains enlarge further. Consequently, a TiC skeletal structure is formed within the sintered specimen.

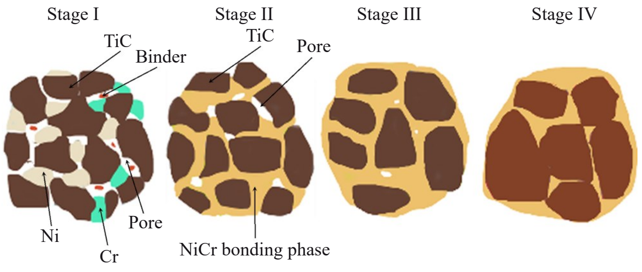

Fig.6 Schematic diagram of densification behavior and microstructure evolution in TiC-NiCr cermet[40]

The fourth stage occurs at 1380–1450 °C (sintering temperature), i. e., the sintering stage, as shown in Fig. 6. After the three stages, the TiC particles are contacted and combined to form a continuous skeleton. The remaining Ni-Cr liquid phase fills the voids in the skeleton. During this stage, the existence of a solid skeleton prevents the further rearrangement of the particles because of its rigidity, resulting in a significant decrease in the densification rate.

3.2 Oxidation resistance of TiC-NiCr

3.2.1 Oxidation kinetic curves

Fig. 7 reveals that during the high-temperature oxidation at 900 °C, the TiC-NiCr metal ceramic exhibits a linear fluctuating growth trend in the initial oxidation period (<500 h). The oxidation mass gain rate accelerates at the onset of oxidation, which is attributed to the dynamic changes in the formation and disruption of the oxide-layer protective layer. In this initial stage, the oxide layer is extremely thin, and because of the short diffusion paths, the atoms participating in the reaction within the matrix easily reach the oxidation reaction interface through the oxide layer, resulting in a faster oxidation rate. With a prolonged oxidation time (>500 h), the mass gain rate is significantly decreased. The oxide layer is thickened and undergoes lateral growth, and the diffusion rate of the ions involved in the reaction is decreased.

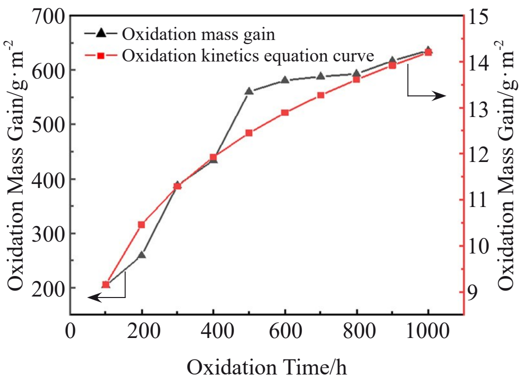

Fig.7 Relationship between oxidation mass gain and oxidation time of TiC-NiCr cermet oxidized at 900 °C

Consequently, the mass gain due to oxidation decreases, and the oxidation rate slows, showing an overall linear growth trend, indicating that as the surface oxide layer gradually thickens, it becomes more stable and denser, reducing the surface porosity and impeding further oxidation. Metal ceramics exhibit improved oxidation resistance. The mass gain results are shown in Table 2. It can be seen that the oxidation mass gain of TiC-NiCr cermet at 900 °C follows an approximately parabolic kinetic pattern over time.

To derive the oxidation equation, the experimental data in Table 2 are processed using the formula $W^n=Kt$ as the fitting equation. The oxidation kinetics equation is then fitted using the least squares method[41], as follows:

$$n \lg W = \lg K + \lg t \tag{2}$$

$$\lg t = n \lg W - \lg K \tag{3}$$

where n is constant, W is oxidation mass gain, K is oxidation kinetic constant, and t is oxidation time.

Substituting the data from Table 2 into Eq. (2) and performing the calculations, the following results can be obtained: n=5.2531 and K=1131.4.

Therefore, the oxidation kinetics equation is $W^{5.2531}=1131.4t$. Fig. 7 also shows this relationship between oxidation mass gain and oxidation time of TiC-NiCr cermet oxidized at 900 °C.

By comparing the mass gain due to oxidation and the oxidation kinetics equation of TiC-NiCr cermet oxidized at 900 °C, it is observed that the actual degree of oxidation is significantly higher than the results from theoretical calculation, and the process is more rapid and intense. The oxidation of metal ceramics is influenced by not only their composition but also two main factors: the density and the protective oxide layer. Density has a significant impact on the oxidation resistance of a material. Oxygen easily permeates through the pores or defects in non-dense materials, thereby accelerating the oxidation reaction rate. The magnitude of the porosity has a noticeable effect on the activation energy of the oxidation process. As the porosity increases, the activation energy decreases, leading to a reduction in the oxidation resistance. The protective oxide layer, formed by a dense oxidation layer, hinders the penetration of oxygen and reduces or prevents material loss. Therefore, enhancing oxidation resistance is important.

3.2.2 Performance changes before and after oxidation

After exposure to high-temperature oxidation at 900 °C, a distinct oxide layer is formed on the surface, which considerably reduces the surface hardness of the TiC-NiCr cermet from 65.5 HRC to 38.0 HRC. After removing the surface oxide layer, the hardness of the specimens is measured after 200, 400, and 800 h as 62.0, 61.0, and 60.5 HRC, respectively. The hardness shows a slight decrease with no significant variation, indicating that the oxide layer plays a protective role. Considering the potential errors in the oxidation tests and hardness measurements, the oxidation test does not affect the hardness of the TiC-NiCr cermet matrix. Fig. 8 illustrates the bending strength variation with oxidation time. The bending strength of the unoxidized specimen is 1300 – 1500 MPa. After oxidation for 1000 h, the minimum bending strength is 790 MPa, indicating the effect of the oxidation process on the bending strength of the material, which is gradually decreased with the prolongation of oxidation time. The bending strength of cermets is closely related to the internal sources of fractures, such as pores. In Fig. 8, a significant inflection point is observed at 300 h, indicating that in the early stage of oxidation, the oxidation not only occurs on the surface of the cermet but also penetrates the material interior through defects, such as pores, leading to an increase in fracture sources and a rapid decrease in bending strength. After oxidation for 300 h, a stable and moderately thick oxide layer forms on the surface, impeding the enlargement or addition of fracture sources and thereby slowing down the decline in bending strength.

3.2.3 Microscopic characteristics of oxide layer

(1) Surface morphology and composition analysis of oxide layer

After oxidation at 900 °C, TiC-NiCr cermets develop a dense brownish oxide layer on the surface, exhibiting a metallic luster. With the prolongation of oxidation time, the color of the oxide layer is deepened, and the layer remains firmly adhered to the surface, demonstrating good integrity. No instances of oxide layer detachment can be observed for any specimen. The morphologies of the surface oxide layer are shown in Fig. 9. Fig. 9 illustrates that the TiC-NiCr cermet generates a substantial amount of irregularly shaped granular oxide on the surface after oxidation at 900 °C (Fig. 9a, 9c, and 9e). Additionally, with the prolongation of oxidation time, the particles are gradually accumulated and enlarged, forming columnar or elongated rutile titanium dioxide, and the connections between particles become progressively tighter (Fig. 9b, 9d, and 9f). XRD analysis of the oxidized surface (Fig. 10) reveals the predominant presence of TiO_2 with a trace amount of $NiTiO_3$. With the prolongation of oxidation time, TiO_2 exhibits enhanced stability, gradually forming a dense oxide layer. The rapidly increase in TiO_2 content inhibits the reaction of $NiTiO_3$, leading to the formation of $NiTiO_3$.

(2) Morphology and composition analysis of oxidation cross-section

Fig. 11 shows the cross-section morphologies of the oxide layer. With the prolongation of oxidation time, the thickness of the oxide layer is noticeably increased from approximately

Table 2 Oxidation mass gain results

Oxidation time, t/h	300	400	500	600	700	800	900	1000
Oxidation mass gain, W/g·m^{-2}	388	434	560	581	588	593	617	636

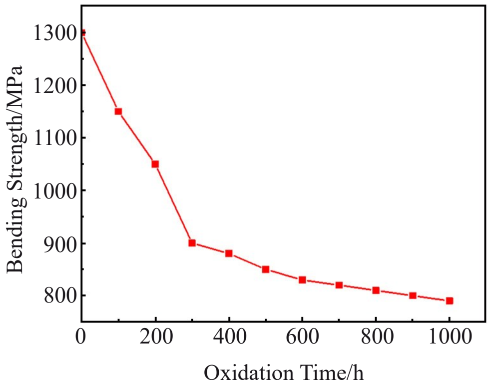

Fig.8 Bending strength variation of TiC-NiCr cermet oxidized at 900 °C

80 μm to around 260 μm with the maximum oxidized impact zone reaching 300 μm in size. A distinct dark oxide layer can be observed, and a matrix structure containing granular titanium carbide can also be observed. The oxide layer is divided into two layers: an outer layer and an inner layer. The outer layer has a loose structure and abundant pores, exhibiting higher Ti and O contents. Combined with XRD analysis, the predominant oxide in the outer layer is TiO_2 with a minor amount of $NiTiO_3$. In contrast, the inner oxide layer is relatively dense. The formation of this dense oxide layer is responsible for the decrease in oxidation rate over time.

As shown in Fig.11a, when the oxidation time is 100 h, the loose structure of the oxide layer is relatively inconspicuous with smaller and less widespread pores. As shown in Fig.11b, after oxidation for 500 h, the loose structure becomes more pronounced, exhibiting numerous and widely distributed pores. Fig.11c shows that after oxidation for 800 h, the loose structure and pore size decrease. Additionally, the bottom of the inner oxide layer exhibits a branched intermittent distribution of the inner oxide layer, penetrating the surface layer of the matrix.

A distinct layered structure of the oxide layer can be observed through the analysis of element distributions, as shown in Fig. 12. The surface oxide layer is primarily composed of Ti and O. XRD patterns in Fig. 13 indicate that the outer oxide layer is predominantly TiO_2 with a minor presence of unoxidized TiC. The inner layer has higher concentrations of Ni and Cr, forming a dense structure with a whitish appearance. In addition, Ni, Cr, and C are enriched at the interfaces between the oxide layers. Fig. 13 also reveals that the main components of the oxide layer are TiO_2, NiO, Cr_2O_3, and a small amount of Ni-TiO_3 and $NiCr_2O_4$. Eq.(4–8) show the related reactions, as follows:

$$TiC(s) + 3/2O_2(g) \rightarrow TiO_5(s) + CO(g) \tag{4}$$

$$Ni(s) + 1/2O_2(g) \rightarrow NiO(s) \tag{5}$$

$$Cr(s) + 3/4O_2(g) \rightarrow 1/2Cr_2O_3(s) \tag{6}$$

$$NiO(s) + TiO(s) \rightarrow NiTiO_3(s) \tag{7}$$

$$NiO(s) + Cr_2O_3(s) \rightarrow NiCr_2O_4(s) \tag{8}$$

The Gibbs free energy of Eq.(4–8) occurring at 900 °C is −1132.46, −180.04, −955.07, −20.74, and −48.33 kJ/mol, respectively. Eq.(4) reveals that during the oxidation process, TiC generates a certain amount of gas, contributing to the formation of pores and loose structures. Thermodynamic analysis indicates that TiC exhibits the highest propensity to react with oxygen, followed by Cr. However, Ni demonstrates the weakest oxidation reaction capability. By investigating the oxidation products of the alloy after oxidation in air at 900 °C, the primary oxides undergo further solid-state reactions, as expressed in Eq.(7–8), leading to the formation of $NiTiO_3$ and a trace amount of $NiCr_2O_4$.

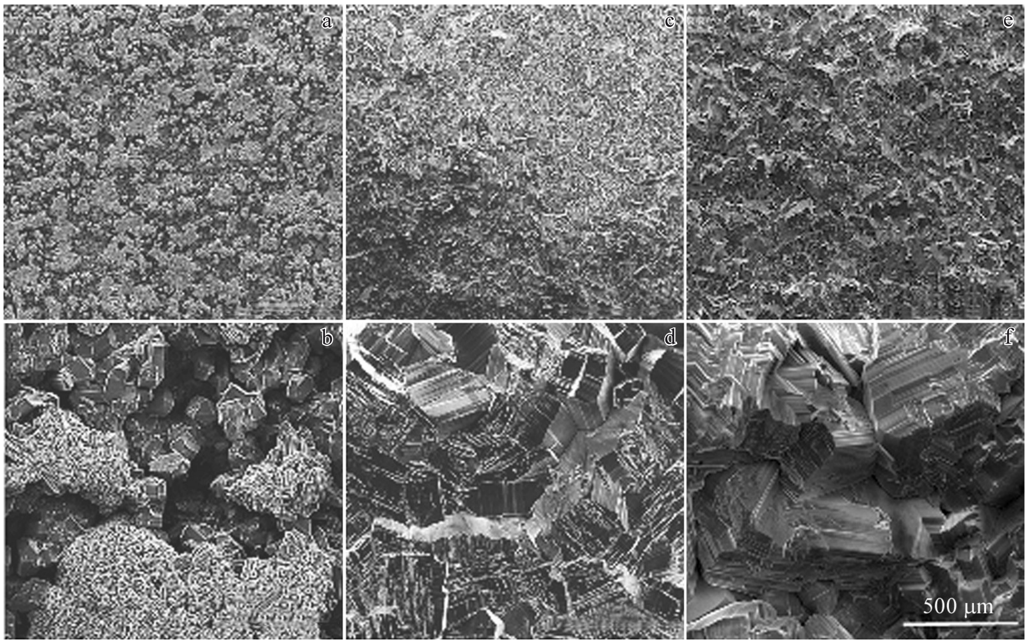

Fig.9 Morphologies of TiC-NiCr cermets oxidized at 900 °C for 200 h (a–b), 500 h (c–d), and 800 h (e–f)

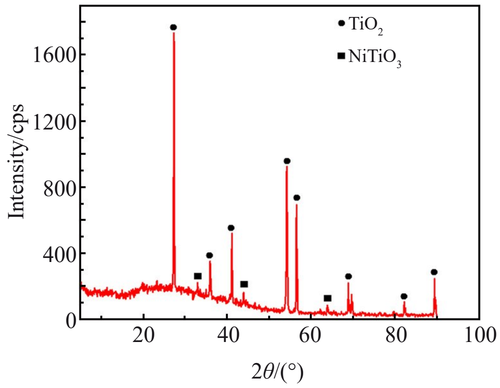

Fig.10 XRD pattern of oxide layer on TiC-NiCr cermet surface after oxidation at 900 °C

(3) Microstructure and compositional analysis of oxidation products

During oxidation for 1100 h, the ongoing reactions lead to the development of cracks and defects in the oxide layer, serving as pathways for the oxidation reaction to progress to deeper layers. Solid-state reactions, such as Eq.(7–8), occur at deeper places, subsequently triggering the continuous advancement of reactions expressed in Eq.(4–6). Consequently, the entire oxidation process gradually intensifies, ultimately resulting in the complete oxidation of the specimen. Therefore, NiO is further consumed during the process. As shown in Fig.14 and Fig.15, the oxide layer is divided into white region (point 1 in Fig.15a) and light-grey region (point 2 in Fig.15a). Fig. 15c reveals that this light-grey region is primarily composed of TiO_2, which is attributed to the considerably higher TiC content compared with that of Ni, resulting in TiO_2 being the predominant final oxidation product. The white region was further analyzed through EDS element mapping, and the results are shown in Fig. 16. It can be seen that the white region contains O, Ti, and Ni, suggesting that the white region is $NiTiO_3$. Notably, owing to the lightweight nature of O atoms in EDS detection, a relatively large deviation may be observed in atomic ratios in the detected results, compared with the anticipated atomic composition of TiO_2 and $NiTiO_3$[42].

The content of Cr_2O_3 is relatively low, and element distribution maps across the cross-section of the oxide layer as well as XRD analysis jointly reveal the predominant presence of Cr_2O_3 at the bottom of the oxide layer. Cr_2O_3 exhibits a linear distribution, gradually forming a relatively continuous and completely layered structure with the prolongation of oxidation time. The analysis of typical oxidation products also indicates a high correlation between the distributions of Cr and O, confirming the presence of Cr_2O_3. Simultaneously, a small amount of Cr is observed at different positions in Fig. 16. Cr_2O_3 primarily nucleates at the grain boundaries on the alloy surface, whereas NiO nucleates across the entire surface. Owing to its rapid growth rate, NiO forms a continuous NiO oxide layer covering the Cr_2O_3 nuclei, resulting in the formation of an external NiO oxide layer (containing Cr_2O_3 particles). As oxidation progresses, Cr_2O_3 gradually forms, and the oxygen partial pressure at the oxide layer/matrix interface rapidly decreases. When the oxygen partial pressure falls below the equilibrium decomposition pressure of NiO, NiO growth ceases. Under severe oxidation conditions, such as temperature of 900 °C and duration of 1100 h, the internal oxidation of Cr occurs because of its low content. Cr_2O_3 particles are formed within the matrix, and as the external oxide layer enters the matrix, most internally oxidized Cr_2O_3 particles are engulfed by NiO. The result of the solid-state reaction is the generation of $NiCr_2O_4$, which forms an outer layer of NiO, an intermediate layer of spinel-type $NiCr_2O_4$, and a very thin inner layer of Cr_2O_3 with a minor occurrence of internal oxidation of Cr.

4 Discussion

4.1 Sintering analysis of TiC-NiCr cermet

The porosity, theoretical density, relative density, and shrinkage of the TiC-NiCr cermet prepared via powder metallurgy are presented in Table 3. The notation A04B00 indicates that the content of A-type pores with sizes smaller than 10 μm is 0.06vol%, and no B-type pores with the size of 10–25 μm exist. This result infers that the specimen exhibits good density after sintering with low porosity, which is attributed to its liquid phase sintering properties. Densification of the cermet relies primarily on the plastic flow of the NiCr metallic phase and the rearrangement of the TiC ceramic phase particles, accompanied by the simultaneous elimination

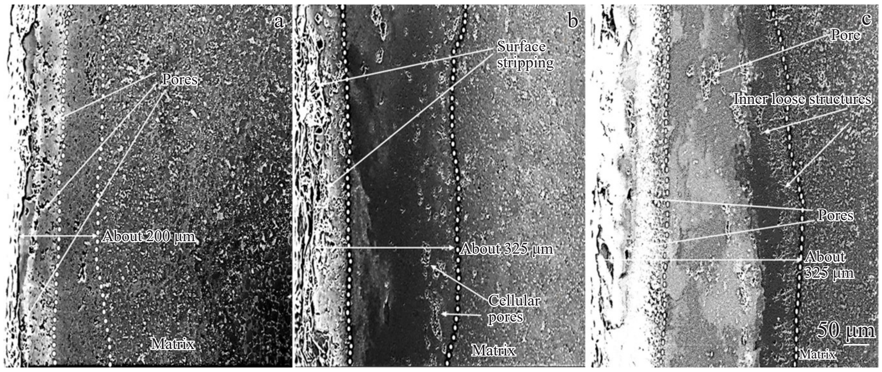

Fig.11 Cross-section morphologies of oxide layers of TiC-NiCr cermet oxidized at 900 °C for 200 h (a), 500 h (b), and 800 h (c)

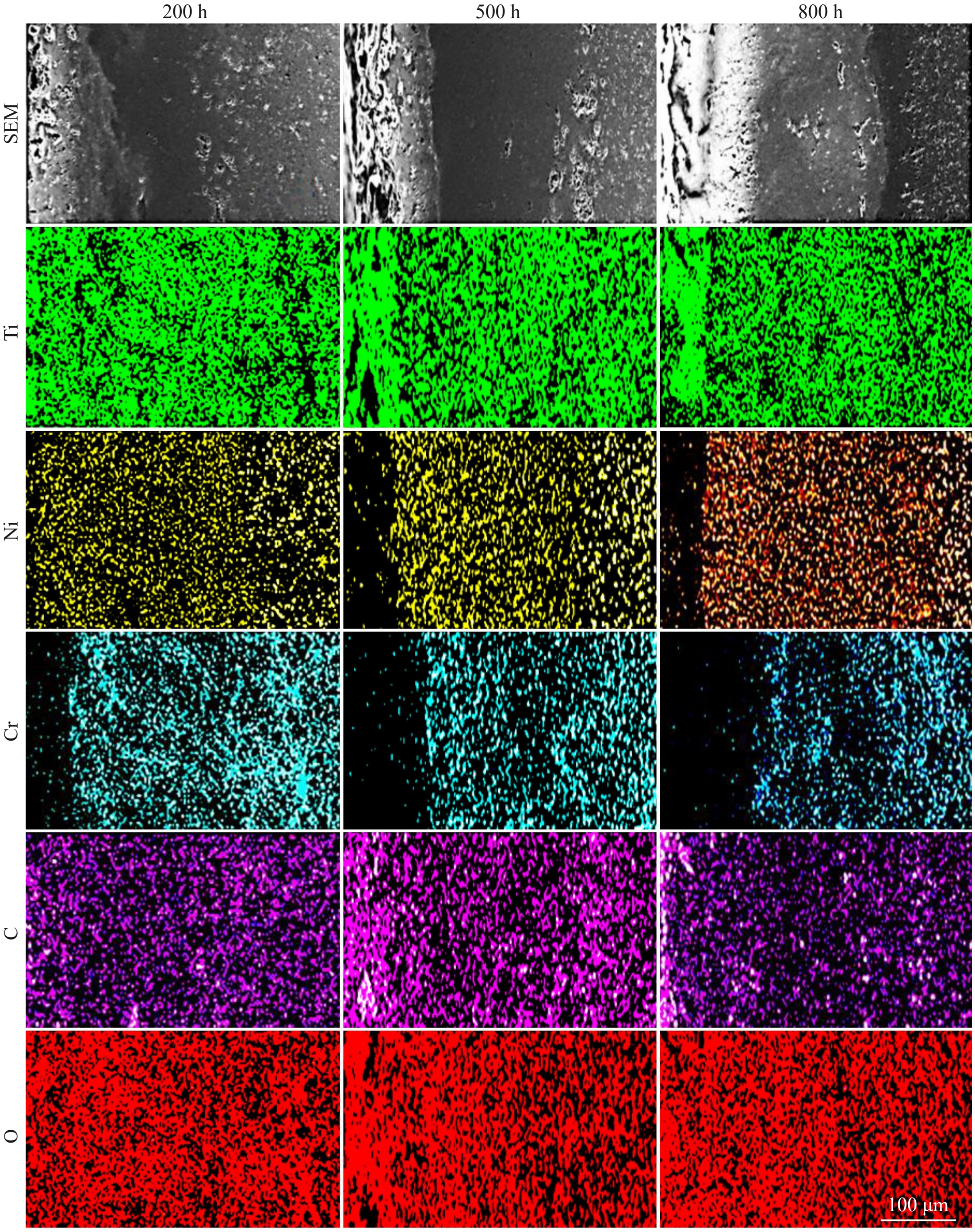

Fig.12 SEM images and EDS element mapping results of oxide layers of TiC-NiCr cermet oxidized at 900 °C for 200 h, 500 h, and 800 h

of voids within the material. The driving forces for densification primarily stem from two aspects: the surface tension of the liquid phase acting on the pores and the capillary forces generated by the liquid phase penetrating solid-phase particles. Liquid phase sintering consists of three stages: flow/dissolution, precipitation of the liquid phase, and sintering of the solid phase. During the stage of liquid phase plastic flow, the particles are rearranged into the most closely packed configuration, rapidly increasing the density of the sintered body. In the rearrangement stage, although pore elimination and particle rearrangement occur swiftly, leading to a rapid densification process, the formation of bridges between particles after they converge to a certain extent introduces increased resistance against the viscous flow of the liquid phase. Consequently, the green compact cannot achieve complete density. Full densification requires the completion of two stages. In the second stage, as the gas pores are essentially eliminated and the particle spacing decreases, infiltration of the liquid phase into the remaining pores becomes more challenging. Hence, compared with the preceding stage, the densification rate slows down. In the third stage, the solid-phase skeleton introduces rigidity, hindering further particle

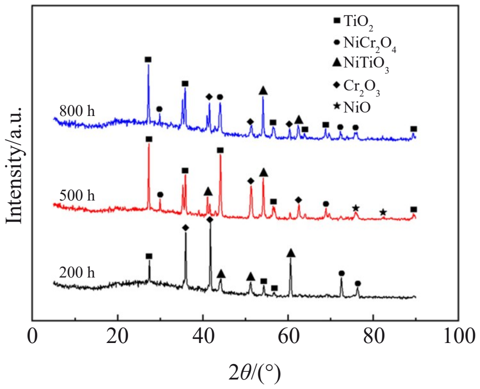

Fig.13 XRD patterns of oxidized surface of TiC-NiCr cermet oxidized at 900 °C for 200 h, 500 h, and 800 h

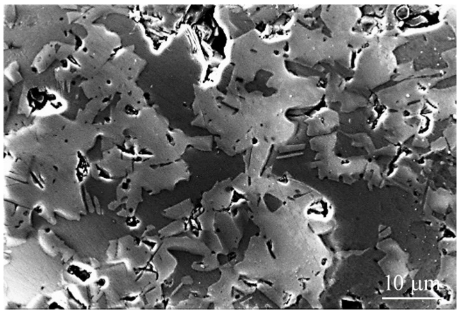

Fig.14 Microstructure of oxide layer of TiC-NiCr cermet oxidized at 900 °C for 1100 h

rearrangement and leading to a significant reduction in the densification rate. The toughness of liquid phase sintering densification in cermet depends on three fundamental conditions related to the properties of the liquid phase: (1) wetting of the NiCr liquid phase on the surface of TiC particles; (2) solubility of the TiC particles in the liquid phase of the NiCr matrix; (3) quantity of the liquid phase at the sintering temperature. Wetting is determined by the surface tensions γ_L and γ_S of the liquid and solid phases, respectively, as well as the interfacial tension γ_{SL} between the two phases. When the NiCr liquid phase wets the TiC particles, the equilibrium thermodynamic condition at the contact point can be obtained by $\gamma_S=\gamma_{SL}+\gamma_{L\cos\theta}$, where θ represents the wetting angle of the liquid phase concerning the solid phase. As the temperature rises, θ gradually decreases[43].

4.2 Oxidation-protective property of coating

Previous studies have indicated that the high-temperature oxidation behavior of the experimental materials is influenced by both kinetic and thermodynamic factors[44]. According to the relevant data in *Handbook of Inorganic Thermodynamics*, the calculation formula of the Gibbs free energy function of the substance under constant pressure conditions during oxidation of the studied alloy is as follows:

$$\Delta G_T^{\ominus} = \Delta H_T^{\ominus} - 298\Delta S_T^{\ominus} \tag{9}$$

where T is temperature, H is enthalpy, and S is entropy.

According to the second law of thermodynamics, the change in the Gibbs free energy serves as a criterion for assessing the spontaneity of a reaction. When ΔG=0, neither forward nor reverse reactions proceed spontaneously. In the case of ΔG>0, the reverse reaction occurs spontaneously; while for ΔG<0, the forward reaction takes place spontaneously. For the oxidation reactions mentioned above, the Gibbs free energy changes remain negative at the oxidation temperature of 900 ° C, indicating that these reactions proceed spontaneously. A lower Gibbs free energy value (negative) signifies a higher priority for the formation of the corresponding oxide. The order of the respective Gibbs free energies for the aforementioned reactions was calculated as follows:

$$\left|\Delta G_{\mathrm{TiC}}^{\ominus}\right| > \left|\Delta G_{\mathrm{Cr}}^{\ominus}\right| > \left|\Delta G_{\mathrm{Ni}}^{\ominus}\right| > \left|\Delta G_{\mathrm{Cr_2O_3}}^{\ominus}\right| > \left|\Delta G_{\mathrm{TiO_2}}^{\ominus}\right| \tag{10}$$

The findings reveal that during the oxidation process, TiC exhibits the highest susceptibility to oxidation, followed by Cr

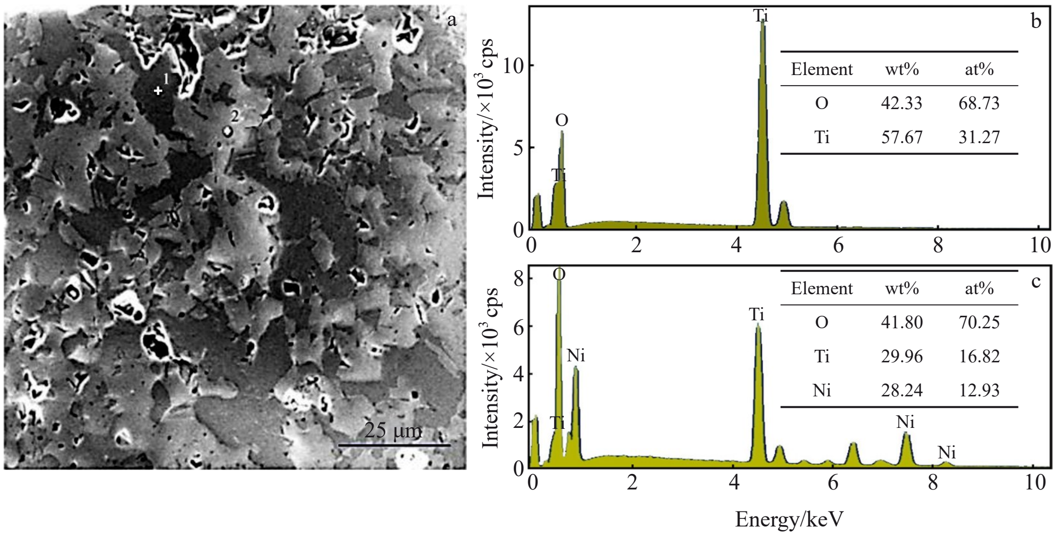

Element	wt%	at%
O	42.33	68.73
Ti	57.67	31.27

Element	wt%	at%
O	41.80	70.25
Ti	29.96	16.82
Ni	28.24	12.93

Fig.15 SEM image of TiC-NiCr cermet (a); EDS analysis results of point 1 (b) and point 2 (c) in Fig.15a

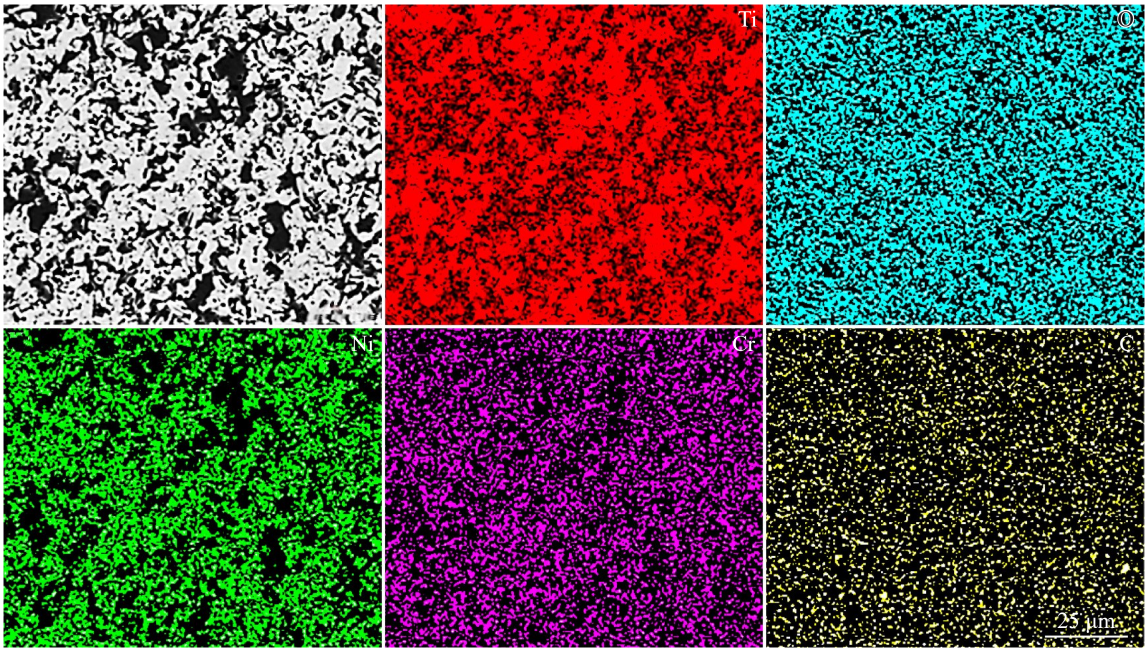

Fig.16 SEM image and EDS element mapping results of white oxidation region

Table 3 Porosity, theoretical density, relative density, and shrinkage ratio of TiC-NiCr cermet

Porosity	Theoretical density/g·cm^{-3}	Relative density	Shrinkage ratio/%
A04B00	6.2	0.98	0.87

and Ni. Subsequently, as the oxidation proceeds after the formation of oxides, internal oxidation compounds, such as $NiCr_2O_4$ and $NiTiO_3$, are generated. Because of its significantly lower Cr content compared with that of Ni, although $NiCr_2O_4$ is relatively facile to form, its content remains low and $NiCr_2O_4$ is primarily distributed in the inner oxidation layer. In summary, the structure of the oxide layer on the surface is determined by both thermodynamic and kinetic factors. Under experimental conditions with elevated oxygen partial pressure, the surface suffers simultaneous oxidation during the initial stages of oxidation. Specifically, TiO_2, NiO, and Cr_2O_3 nucleate simultaneously with TiO_2 rapidly nucleating across the entire surface, which forms a continuous TiO_2 oxide layer covering the cores of NiO and Cr_2O_3. This layer impedes the inward diffusion of oxygen and the outward diffusion of Cr and Ni matrices. As oxidation proceeds, the thickness of the oxide layer continues to increase, and spinel-type oxides continue to form. The oxygen partial pressure at the interface between the oxide layer and matrix rapidly decreases, leading to the gradual cessation of the oxidation process.

5 Conclusions

1) A uniform densely packed ceramic material with excellent properties can be achieved by strictly controlling the raw material quality and optimizing the process parameters. The sintering process of TiC-NiCr cermet involves liquid phase sintering, ultimately resulting in a dense structure with TiC particles uniformly distributed within the NiCr matrix.

2) After high-temperature oxidation at 900 °C, a dense oxide layer is formed on the surface of the TiC-NiCr cermet surface. Although no significant change can be observed in the hardness of the inner layer, the overall bending strength decreases. The TiC-NiCr cermet exhibits passivation during oxidation, and the dense oxide layer enhances the high-temperature oxidation resistance. However, the oxidation products are unstable with possible further oxidation of Ni and Cr. Therefore, the oxidation over approximately 1000 h can lead to substantial material deterioration.

3) The oxidation mass gain of TiC-NiCr cermet at 900 °C follows an approximately parabolic kinetic pattern over time. When the oxidation time is 500 h, the oxidation mass gain rate is relatively rapid before gradual stabilization, suggesting that the initial growth of the oxide layer hinders further oxidation. The oxidation process is characterized by passivation, and the formation of an oxide layer contributes to enhanced oxidation resistance.

4) During oxidation at 900 °C, TiC-NiCr cermet forms an outer layer primarily composed of relatively porous TiO_2/NiO with a small amount of Cr_2O_3. The inner layer consists of a continuous and dense composite oxide layer, including TiO_2/$NiTiO_3$/$NiCr_2O_4$/Cr_2O_3. This composite oxide layer impedes the outward diffusion of Ni and Cr from the matrix, reducing the oxidation rate and ultimately hindering oxidation penetration into the material.

5) The high-temperature oxidation behavior of the TiC-NiCr cermet is influenced by both kinetic and thermodynamic factors. TiC is the most prone to oxidation, followed by Cr and Ni. With the prolongation of the oxidation time after the formation of the oxides, internal oxidation compounds, such as $NiCr_2O_4$ and $NiTiO_3$, are generated. However, owing to the significantly lower content of Cr compared with that of Ni in the composition, although $NiCr_2O_4$ forms relatively easily, its content remains low and it is primarily distributed in the inner oxidation layer.

References

1 Zhou Yu. *Ceramic Materials Science*[M]. Beijing: Science Press, 2004: 3 (in Chinese)

2 Ettmayer P, Lengauer W. *International Journal of Powder Metallurgy*[J], 1989, 21(2): 37

3 Dingerpov J R, Crandall W B, Jin S. *Cermet*[M]. Shanghai: Shanghai Science and Technology Press, 1964: 2

4 Jiang Yuhe. *Chemistry of Nonmetallic Materials*[M]. Beijing: Science and Technology Literature Press, 1992: 2 (in Chinese)

5 Xu Qiang, Zhang Xinghong, Qu Wei et al. *Cemented Carbide*[J], 2002, 19(4): 221

6 Yan Kangping. *Engineering Materials*[M]. Beijing: Chemical Industry Press, 2001: 264 (in Chinese)

7 Mu Baichun. *Strengthening and Toughening of Ceramic Materials*[M]. Beijing: Metallurgical Industry Press, 2002: 16 (in Chinese)

8 Liu Ning, Liu Xuesong, Ye Jingfeng *et al. Ti(C, N) -based Cermets*[M]. Hefei: Hefei University of Technology Press, 2009: 9 (in Chinese)

9 He Congxun, Xia Zhihua, Wang Youming *et al*. *Rare Metals*[J], 1999, 23(1): 77 (in Chinese)

10 Hu Wenbin, Zhang Long, Wang Jianjiang *et al. Materials Reports*[J], 2010, 24(23): 29 (in Chinese)

11 Liu Tao, Feng Ping. *Jiangsu Ceramics*[J], 2005, 38(6): 20 (in Chinese)

12 Xiao Shuiqing, Wu Shanghua. *Cemented Carbides*[J], 2014, 31(2): 112 (in Chinese)

13 Wu H, Zheng Y, Zhang J J *et al. Ceramics International*[J], 2019, 45(17): 22371

14 Yu H Z, Liu W J, Feng P *et al. International Journal of Refractory Metals and Hard Materials*[J], 2014, 45: 48

15 Ren X, Yu L, Liu Y *et al. International Journal of Refractory Metals and Hard Materials*[J], 2016, 61: 207

16 Wang Qinsheng. *Superhard Materials and Products*[M]. Zhengzhou: Zhengzhou University Press, 2006 (in Chinese)

17 Zhao Min. *Stone*[J], 2016(2): 25 (in Chinese)

18 Mancisidor A, Lunobilbao C, Vielma N J *et al. Powder Metallurgy*[J], 2014, 56(5): 362

19 Atefeh Aramian, Seyed Mohammad Javad Razavi, Zohreh Sadeghian *et al*. *Additive Manufacturing*[J], 2020, 33: 101130

20 Zhang Fenglin, Wang Chengyong, Song Yuexian. *Powder Metallurgy Technology*[J], 2003, 21(4): 236 (in Chinese)

21 Wang Guodong. *Cemented Carbide Principle*[M]. Beijing: Metallurgical Industry Press, 1988: 13 (in Chinese)

22 Liu Yong, Yang Jiangao. *Gradient and New Structure Cemented Carbide*[M]. Changsha: Central South University Press, 2010: 22 (in Chinese)

23 Li D, Liu Y, Ye J W *et al. International Journal of Refractory Metals and Hard Materials*[J], 2021, 97(1): 105518

24 Lu Z Y, Du J, Sun Y J *et al. International Journal of Refractory Metals and Hard Materials*[J], 2021, 97: 105516

25 Gao Y, Yan M Y, Luo B H *et al. Materials Science and Engineering A*[J], 2017, 687: 259

26 Pastor H. *International Journal of Refractory Metals and Hard Materials*[J], 1987, 6(4): 196

27 Hisashi Suzuki, Koji Hayashi, Hideaki Matsubara. *Journal of Japan Metal Society*[J], 1983, 22(4): 312

28 Yan Xifeng, Wang Haibin, Liu Xuemei *et al*. *Journal of the European Ceramic Society*[J], 2019, 39(10): 3023

29 Hayness W M. *CRC Handbook of Chemistry and Physics*[M]. London: CRC Press, 2016

30 Parikh N M, Humenik J R. *Journal of the American Ceramic Society*[J], 1957, 40(9): 315

31 Yang Jia, Li Kui, Tang Aitao *et al*. *Materials Reports*[J], 2003, 17(8): 44 (in Chinese)

32 Wang Panxin. *Powder Metallurgy*[M]. Beijing: Metallurgical Industry Press, 1997 (in Chinese)

33 Wang Shisen. *Special Ceramics*[M]. Changsha: Central South University Press, 2005 (in Chinese)

34 Dalai R P, Das S, Das K. *Canadian Metallurgical Quarterly*[J], 2014, 53(3): 317

35 Wang Quanzhao, Liu Yue, Guan Dehui *et al*. *Acta Metallurgica Sinica*[J], 2005, 41(11): 1121 (in Chinese)

36 Sun Wenli. *Study on the Preparation, Microstructure and Properties of Ti(C, N) -NiCr-based Ceramics*[D]. Wuhan: Huazhong University of Science and Technology, 2012 (in Chinese)

37 Ma Hui, Luo Ji. *Powder Metallurgy Technology*[J], 2021, 39(2): 147 (in Chinese)

38 Teng Jianwei. *Effect of Co, Ti Addition on Microstructure and Properties of Ni-Cr-W-based Superalloy by Powder Metallurgy*[D]. Changsha: Central South University, 2022 (in Chinese)

39 Feng Fan, Fan Jinglian, Cheng Huichao *et al*. *Materials Science and Engineering of Powder Metallurgy*[J], 2012, 17(4): 408 (in Chinese)

40 Dai Wenjie, Pan Shiyan, Shen Xiaoping. *Materials Reports*[J], 2019, 33(9): 2929 (in Chinese)

41 Yao Zhenhua. *High Temperature Oxidation Behavior of Ti(C, N) -Based Cermets*[D]. Wuhan: Huazhong University of Science and Technology, 2007 (in Chinese)

42 Li Lingqun, Fan Jinglian, Tian Jiamin *et al*. *Materials Science*

and Engineering A[J], 2021, 819: 141442

43 Dai J J, Zhu J Y, Chen C Z *et al. Journal of Alloys and Compounds*[J], 2010, 685: 784

44 Meredith B, Milner D R. *Powder Metallurgy*[J], 2016, 19(3): 62

TiC-NiCr金属陶瓷的制备与高温氧化性能

张 雷[1,2,4]，黄本生[1]，解传娣[2,4]，陈 根[5]，杜 皎[2,4]，孙海身[2,3,4]，左寒阳[6]

(1. 西南石油大学 新能源与材料学院，四川 成都 610500)
(2. 山东省粉末冶金先进制造重点实验室，山东 济南 271100)
(3. 北京科技大学，北京 100083)
(4. 莱芜职业技术学院 智能制造系，山东 济南 271100)
(5. 昆山安意源管道科技有限公司，江苏 昆山 215300)
(6. 四川省材料腐蚀与防护重点实验室，中国 自贡 643002)

摘 要：采用粉末冶金法制备TiC-NiCr金属陶瓷，并对其在900 ℃下的氧化行为进行了研究。结果表明，TiC-NiCr结构均匀，具有优异的力学性能，硬度为65 HRC，抗弯曲强度为1450 MPa。利用X射线衍射仪和扫描电子显微镜研究了TiC基陶瓷的高温氧化机理。加入的Ni和Cr元素及其固溶体不仅与硬相TiC结合，保证了金属陶瓷的物理性能，而且通过形成致密的复合氧化层，阻碍了氧化过程中的内部扩散，从而增强其抗氧化性。TiC-NiCr金属陶瓷在900 ℃下呈现出致密的氧化保护膜，可连续氧化约1000 h。提出了一种制备TiC-NiCr金属基复合材料的方法，并对其抗氧化性能进行了评价，为在降低生产成本的同时提高其力学性能和抗氧化性能提供了理论和实践依据。

关键词：TiC-NiCr；微观组织；高温氧化；热力学与动力学

作者简介：张 雷，男，1984年生，博士，西南石油大学新能源与材料学院，四川 成都 610500，E-mail：zhanglei200303@163.com